



# A fast simulation method for thermal management in wire arc additive manufacturing repair of a thin-walled structure

Paul Qvale<sup>1</sup> · Eirik B. Njaastad<sup>2</sup> · Torgeir Bræin<sup>3</sup> · Xiaobo Ren<sup>4</sup>

Received: 28 November 2023 / Accepted: 9 March 2024 / Published online: 21 March 2024  
© The Author(s) 2024

## Abstract

Ensuring first-time-right on-site repair of critical structures is a key challenge for additive manufacturing (AM)–based repair solutions. Fast thermal simulations are thus needed to plan efficient and error-free AM processes. This paper addresses a fast thermal simulation method for a novel subsea wire arc additive manufacturing (SWAAM) repair procedure. Current commercial finite element (FE) codes for typical welding and AM are computationally expensive and slow. The presented 2D finite difference approach can be used to simulate SWAAM on a damaged plate with around 70 times acceleration compared to real welding times, without the use of parallelization. Although not being able to accurately represent the temperature in close vicinity of the welding torch, the approach shows excellent correspondence with FE simulations and experiments in regions of the plate where the temperature has assumed a distribution that is largely two-dimensional. Compared with FE simulations, the approach is experimentally verified to be accurate to 10 °C within 7 s after the welding torch has passed a point on the plate. Thus, the approach can provide a measure of the global temperature field in a thin-walled structure during repair. The thermal simulation is preceded by a welding path planner, which generates appropriate paths based on slicing of a 3D surface scan of the damage that is to be repaired. Damages to equipment or non-ideal welding conditions are prevented by automatically pausing the welding if the calculated temperature in the path ahead of the welding torch exceeds a predefined interpass temperature limit.

**Keywords** Wire arc additive manufacturing · Thermal simulation · Numerical methods · Welding path planning · On-site subsea repair

## 1 Introduction

Subsea wire arc additive manufacturing (SWAAM) is a novel additive manufacturing process that uses conventional hyperbaric welding [1] to build or repair parts under water, which is an extension of the classic wire arc additive manufacturing

(WAAM) method [2]. WAAM technology adopts an electric arc as a heat source and wire as feedstock in the additive manufacturing (AM) process to build metallic parts. Compared to other AM processes, WAAM is characterized by its ability to build large metallic components with less constraints and relatively high deposition rates, e.g., 2–3 kg/h using cold metal transfer (CMT)-based WAAM process [3]. Moreover, the WAAM process can be easily robotized, and the system is relatively portable, making it applicable for on-site repair. Repair of damaged components and structures to extend their lifetime is becoming more and more attractive, considering the increasing focus on sustainability and reduced CO<sub>2</sub> emissions [4]. Furthermore, repairing a damaged component rather than replacing it with a brand-new one can offer substantial economic savings due to decreased downtime and lead time. Examples of candidates for WAAM repair are components that are worn, eroded or corroded, where the original component geometry can be restored by building from the damaged surface.

✉ Paul Qvale  
paul.qvale@sintef.no

<sup>1</sup> Department of Materials and Nanotechnology, SINTEF Industry, P.O.Box 4760 Torgarden, Trondheim NO-7465, Norway

<sup>2</sup> Department of Production Technology, SINTEF Manufacturing AS, P.O.Box 4766 Torgarden, Trondheim NO-7465, Norway

<sup>3</sup> Kongsberg Ferrotech, P.O.Box 1027, Kongsberg NO-3601, Norway

<sup>4</sup> Department of Metal Production and Processing, SINTEF Industry, P.O.Box 124 Blindern, Oslo NO-0314, Norway

During the past years, Kongsberg Ferrotech has developed a robotic system with a unique habitat technology that can establish a controllable environment in situ, e.g., pressure, temperature, and gas composition, including subsea. This enables the use of the SWAAM process for repair. The robotic system can carry all required inspection, machining and AM printing tools to the desired location. For such repairs, it is vital first to understand all relevant details of the damage. Performing the SWAAM repair quickly while staying within the operational window is crucial to minimize component repair time and downtime. Thermal simulations can provide a basis for process time optimization and be used to plan a high-quality repair prior to performing the work.

To minimize the service time, simulations need to be performed while the robotic system is on location. This requires the calculation time to be reduced to a minimum, while maintaining sufficient accuracy. Commercial software codes for welding and AM simulation use 3D finite elements (FE) and high requirements on convergence near the heat source [5, 6], which results in long computation times [7]. In addition, time-consuming modeling tasks to create the FE models have to be manually performed. Some studies have already been published for developing computationally more efficient models for WAAM [8–10]. It has been shown that computational times can be reduced significantly for geometries produced by single-pass directed energy deposition (DED) techniques by using a semi-analytical method [11]. Recently, a neural network has been employed to predict temperature fields during WAAM much faster than what is possible using FE simulations [12]. The current article presents a physics-based numerical method for determining temperature fields in thin-walled structures (i.e., where the thickness is small compared to other dimensions) during WAAM repair. From this, limits for an operational window can be set to avoid overheating and unwanted material properties. The proposed method is applicable to thin-walled structures both above and below the water line, e.g., chemical process equipment, wind turbine towers and ship hulls.

The temperature field from a surface heat source in a thin-walled structure quickly assumes a distribution that is largely two-dimensional [13]. This can be exploited for dimensional reduction of a simulation model when the global and delayed temperature response is of primary interest. In the current work, the finite difference method and a 2D geometric model were used for the thermal simulation of WAAM repair on a test case. The results were used to control that the maximum allowed *interpass temperature limit* was never exceeded during the repair process. Automatic control of a WAAM process based on simulated interpass temperatures was also the topic of a previous study [14], which relied on commercial FE software.

In the current work, the damaged component was scanned with a 3D surface scanner prior to the simulation. Using

knowledge of the nominal wall thickness of the structure, a geometry model could be automatically derived from the surface scan. Welding paths were also generated based on the surface scan. It will be shown that the simplified simulation method yielded appropriate accuracy for the current case and that results were produced considerably faster than with commercial FE software.

In the proceeding Sect. 2, the methodology of the current work is presented. The section is divided into three parts: First, examples of relevant field cases are discussed, and simplifications made to derive a demonstration laboratory case are described. Then, the simplified simulation approach, referred to as the *WAAM repair simulator*, is presented. The subsection describes a procedure for the acquisition of the damaged surface, the welding path planner, the thermal simulation, and how the simulation can be used for decision-making. Finally, procedures for carrying out model validation by results comparison to conventional AM simulations in the Abaqus FE software and an experimental test are presented. In Sect. 3, the validation results are presented and discussed. Sections 4 and 5 summarize some outlines for future work and the conclusions, respectively.

## 2 Methodology

### 2.1 Relevant field cases and demonstration geometry

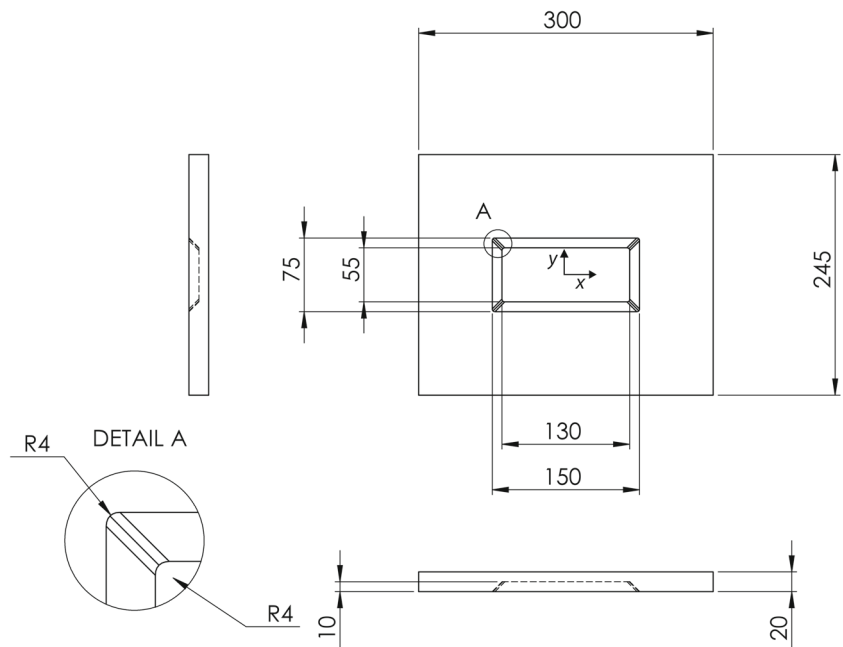
In the current work, two example field cases of damage on a steel subsea pipeline have been considered for SWAAM repair: (1) a dent, where the pipe wall has been pressed inwards and slightly deformed; and (2) exterior corrosion surface damage. The two cases are topologically identical, and both have a missing volume that must be filled to restore the original outside surface. The difference between them is that the corrosion damage involves a reduction of wall thickness. If neglecting the minor spatial differences but considering the thickness distribution, the two cases can be represented by the same type of 2D thermal model.

To demonstrate the viability of the simplified thermal simulation approach, an idealized planar test plate geometry shown in Fig. 1 has been proposed. With its varying thickness, it is representative of the second field case of exterior corrosion surface damage.

### 2.2 WAAM repair simulator

This section presents the simplified simulation approach, the WAAM repair simulator. The following describes the procedure for acquiring the geometry of the damaged surface, the automated path planning for welding, the thermal simulation, and how the simulation can be used for decision-making.

**Fig. 1** Technical drawing of the test plate geometry. “TC” marks the location of a thermocouple



**2.2.1 Surface acquisition**

The input to the WAAM repair simulator is 3D scan data, from which a mesh representation of the surface is created. The surface geometry of the damage is acquired using a profile laser scanning system or 3D camera, which outputs a 3D point cloud in the robot coordinate frame. Once the point cloud is acquired, the next step is to segment and subsample the data before a surface mesh is generated. The expected surface location delimits the segmentation, while subsampling is performed spatially such that the final point cloud has a minimum point distance of 1 mm. The subsampling process reduces the overall data size while maintaining the accuracy of the surface representation. A mesh representation of the surface is generated using planar Delaunay triangulation, which creates a surface mesh by connecting adjacent points in the point cloud.

**2.2.2 WAAM toolpath planning**

Once the surface mesh is generated from the 3D scan of the dented plate, the toolpath for the additive repair process is automatically planned. The algorithm for AM toolpath planning slices the mesh resulting from the 3D scan into layers, each including a perimeter weld path and an infill raster scanning WAAM pattern. The input parameters for the toolpath planning include layer height, string spacing, perimeter to boundary offset, and offset between perimeter and infill. The welding order is also planned based on the welding position to enhance further and generalize the toolpath planning.

The slicing algorithm divides the surface into parallel planes, each spaced by the desired layer height. The intersec-

tion of each plane with the surface mesh produces a series of closed loops representing each layer’s perimeter tool paths. The relation  $n_{layers} = \left\lceil \frac{z_{max} - z_{min}}{t_{layer}} \right\rceil$  is used to calculate the number of required layers, where  $n_{layers}$  is the number of planned layers,  $z_{max}$  and  $z_{min}$  are the maximum and minimum points of the surface scan in the  $z$ -direction, respectively, and  $t_{layer}$  is the desired layer thickness. The infill toolpath of each sliced layer involves creating a zig-zag raster pattern within the boundary of the repair area. The zig-zag raster pattern is generated using a grid that specifies the  $x$  and  $y$  values for each point in the pattern, considering the user-set string spacing  $s$  and path resolution  $r$  parameters.

The resulting zig-zag raster pattern can be represented by a set of line segments  $L_i$ , where  $i = 0, \dots, n$  and each line segment is defined by a set of  $(x, y)$  points  $P_{i,j}$ , where  $j = 0, \dots, m_i$ . If the raster direction is in the longer width direction, the  $x$  and  $y$  values for each point in the zig-zag raster pattern can be calculated as follows:

$$(x_{i,j}, y_{i,j}) = \begin{cases} (\frac{w}{2} + \frac{j-1}{s}, \frac{i-1}{r}) & \text{if } i \text{ is odd} \\ (w - \frac{j-1}{s} - \frac{w}{2}, ir) & \text{if } i \text{ is even} \end{cases} \quad (1)$$

The  $x$  values are determined by adding the string spacing  $s$  to the previous  $x$  value for odd indices and subtracting  $s$  from the previous  $x$  value for even indices. The  $y$  values are determined by multiplying the row index  $i$  by the path resolution  $r$ . The line segments  $L_i$  can be defined by connecting adjacent points in the zig-zag raster pattern:

$$L_i = P_{i,j}, P_{i,j+1}, \text{ for } j = 0, \dots, m_i - 1 \quad (2)$$

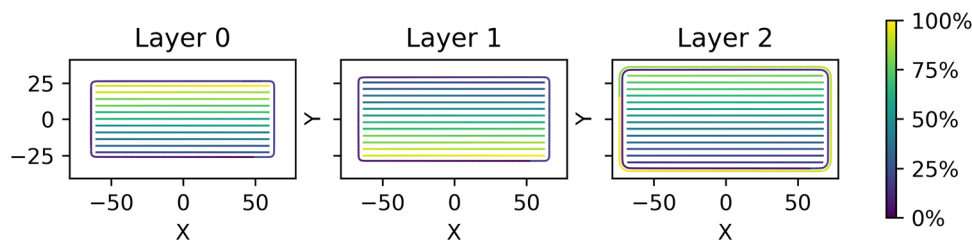


**Fig. 2** The welding path plan for the test plate geometry used for the experiments in the current work. Three layers were necessary for the WAAM repair of the damage in the test plate. The path color represents the planned direction of execution from the start (0%) to the finish (100%)

where  $m_i$  is the number of points in row  $i$ .

Finally, the toolpath data is exported in a format that can be input into the thermal simulations and the SWAAM repair robot system. The exported data includes the tool paths for each layer and deposition parameters such as the heat input and wire feed rate. The resulting tool path plan is illustrated in Fig. 2 for the test plate geometry studied in this work.

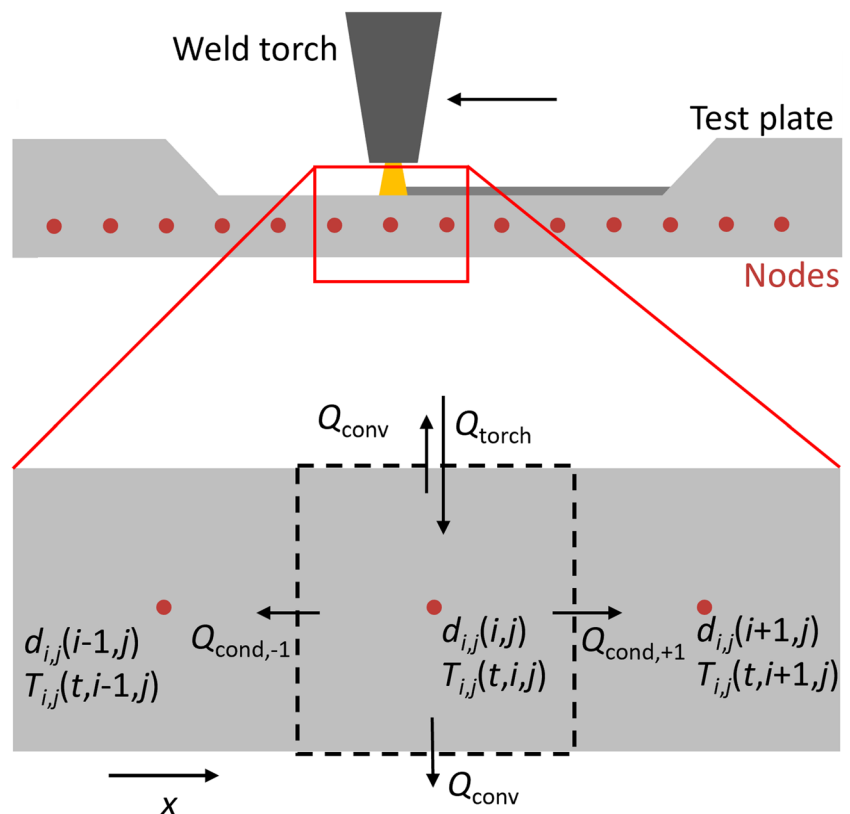
### 2.2.3 Thermal simulation

When heat spreads radially from a point heat source on the surface of a thin-walled structure, the through-thickness gradient of the temperature field quickly diminishes at a distance from the heat source. If the structure is surrounded by air, heat will also accumulate at the surface and “reflect” back into the

more conductive metal, further reducing in-plane temperature gradients. This two-dimensional state of the temperature field is taken advantage of to reduce dimensions of the thermal simulation.

The 2D thermal simulation is based on maintaining the balance of heat,  $Q$ , in each material element in the test plate. Material elements are represented by nodes  $i, j$  in a 2D grid in the plane of the plate, having a thickness  $d(i, j)$  and a temperature  $T(t, i, j)$ . For a plate that is simply dented, the nominal wall thickness  $D$  would be assigned to all nodes, i.e.,  $d(i, j) = D$ . Figure 3 shows an idealized drawing of a cross-section of the test plate. Quantities that describe the boundary between element  $i, j$  and  $i + 1, j$  have been denoted by a subscript +1, instead of the longer  $i, j \rightarrow i + 1, j$ .

**Fig. 3** Model overview of heat transfer between an element and neighboring elements, as well as to the surroundings. Heat transfer to out-of-plane elements has been omitted for clarity



For each element, the temperature can be calculated from the following set of equations, derived from fundamental heat transfer relations:

$$\frac{dQ_{\text{torch}}}{dt} = \frac{dW}{dt} \eta, \tag{3}$$

$$\frac{dQ_{\text{conv}}}{dt} = h(T)\Delta T_{\text{ext}}A_{\text{ext}} = h(T)\Delta T_{\text{ext}}\Delta x \Delta y, \tag{4}$$

$$\frac{dQ_{\text{cond},+1}}{dt} = \frac{k(T) + k(T_{+1})}{2} \frac{\Delta T_{+1}}{\Delta x} A_{+1} = \frac{k(T) + k(T_{+1})}{2} \frac{\Delta T_{+1}}{\Delta x} d_{+1} \Delta y, \tag{5}$$

$$\frac{\partial T}{\partial t} = \frac{\sum \frac{dQ}{dt}}{C} = \frac{\sum \frac{dQ}{dt}}{c\rho V} = \frac{\sum \frac{dQ}{dt}}{c\rho d \Delta x \Delta y}. \tag{6}$$

The nomenclature for Eqs. 3–6 is given in Table 1. Equation 5 has equivalents for all other neighboring elements  $(i-1, j)$ ,  $(i, j+1)$ , and  $(i, j-1)$ , and Eq. 4 can accommodate different cooling media or conditions on each side of the plate, by using different values of  $h$ .

Heat transfer by radiation from the plate surfaces was not expressed explicitly in the current model in order to reduce the number of variables to calibrate. However, if radiative effects are not actively excluded when deriving  $h$  from experiments, they can be thought of as being implicitly included in the model. It is possible to separate convective and radiative

heat transfer by employing a radiation law on the element surfaces in Fig. 3.

Phase transformations can introduce great nonlinearities in the specific heat capacity,  $c(T)$ . In the current work, temperature dependencies on  $c$  were disregarded for two reasons: Firstly, as will be shown, the current 2D approach considers the *average* temperature through the wall thickness. This temperature will likely not reach the melting temperature for large regions of the component. Thus, the greatest nonlinearity in  $c$ , the latent heat of fusion, will have little impact on simulation results. Secondly, abrupt changes in  $c$  can only be captured if the temperature resolution in the simulation is high. This has the potential to slow down the simulation considerably.

**Table 1** Nomenclature for heat transfer Eqs. 3, 4, 5 and 6

Symbol	Definition
$A_{+1}$	Area of the element surface shared with element $(i + 1, j)$
$A_{\text{ext}}$	Area of one external element surface
$C$	Heat capacity
$c$	Specific heat capacity
$d_{+1}$	Thickness of the element surface shared with element $(i + 1, j)$
$h$	Heat transfer coefficient (HTC)
$k$	Thermal conductivity
$Q_{\text{cond}}$	Conductive heat
$Q_{\text{conv}}$	Convective heat
$Q_{\text{torch}}$	Torch heat
$T$	Temperature
$T_{+1}$	Temperature of element $(i + 1, j)$
$\Delta T_{+1}$	Difference to temperature of element $(i + 1, j)$
$\Delta T_{\text{ext}}$	Difference to ambient temperature
$t$	Time
$V$	Volume
$W$	Work
$\eta$	Welding arc efficiency
$\rho$	Density

**Algorithm 1** Pseudocode for path planning, thermal simulation, and decision making.

```

1: Variables ← material properties, boundary conditions, thermal analysis settings, slicing plane normal direction, slicing height step, weld string spacing, boundary and infill offsets, waypoint height, welding wire stick-out, welding parameters, welding and travel speeds and accelerations
2: Load surface mesh from 3D scan
3: Slice the mesh into layers with height  $t_{\text{layer}}$ 
4: for  $i = 1$  to  $n_{\text{layers}}$  do
5:   Generate perimeter weld path for layer  $i$ 
6:   Generate infill raster scanning pattern for layer  $i$ 
7: end for
8: Add waypoints and welding parameters to paths
9: Make trajectories for the welding and waypoint movements
10:  $t \leftarrow 0$ 
11:  $d(i, j) \leftarrow$  surface scan
12:  $T(t, i, j) \leftarrow$  ambient temperature
13: while welding is ongoing do
14:   Locate torch from path
15:   Calculate  $\Delta T(i, j)$  during  $\Delta t$  according to Eqs. 3-6
16:   acceptance flag ← off
17:   while acceptance flag is off do
18:     if  $\max(\Delta T(i, j)) >$  allowed then
19:        $\Delta t \leftarrow \Delta t \cdot$  low factor, where low factor  $< 1$ 
20:        $\Delta T(i, j) \leftarrow \Delta T(i, j) \cdot$  low factor, where low factor  $< 1$ 
21:     else
22:        $t \leftarrow t + \Delta t$ 
23:        $\Delta t \leftarrow \Delta t \cdot$  high factor, where high factor  $> 1$ 
24:       acceptance flag ← on
25:     end if
26:   end while
27:   if checkpoint time is passed then
28:      $(m, n) \leftarrow$  checkpoint location
29:     if welding is ongoing then
30:       if  $T(t, m, n) >$  interpass temperature limit then
31:         Initiate welding pause
32:       end if
33:     else if welding is paused then
34:       if  $\max(T(t, i, j)) <$  low temperature limit then
35:         Terminate welding pause
36:       end if
37:     end if
38:   end if
39: end while

```

The simulation advances by means of the (forward) Euler method using explicit-time integration. A pseudocode covering the path planner, thermal simulation, and decision-making is presented in Sect. 2.2.4.

The accuracy of the simulation is controlled by employing a maximum allowed temperature change in any element from one time increment to the next. To shorten computation times, the heat from the welding torch was distributed to multiple elements by employing a Gaussian filter with a standard deviation of 2 mm on the point heat source following the welding path. The Gaussian distribution for the heat source was regarded chosen due to its intuitive application to a 2D heat field.

In the current simulation model, it was assumed that the plate thickness does not change during the course of the welding process. Neglecting the heat capacity of the added material will lead to an overestimation of the temperature, especially for thick repairs, but this is considered conservative for the current application. Employing a time-dependent thickness function,  $d = d(t, i, j)$ , based on a material deposition model would increase accuracy but also require estimation of the weld bead shapes. This would also allow for simulating repairs of through-thickness holes, which implies updates to the topology of the plate. A material deposition model for WAAM will be presented in an upcoming paper.

### 2.2.4 Path decision making based on the temperature field

Enforcing a maximum interpass temperature limit during a welding operation is widely used [15, 16] as a means to control material microstructure evolution and material properties of the weld, such as the impact energy [17, 18]. As detailed in the pseudocode in Algorithm 1, the WAAM repair simulator monitors the temperature ahead of the torch on the welding path. If the registered interpass temperature is too high, the robot will pause, and the torch turn off until the temperature is low enough to restart welding. By calculating the temperature prior to the repair operation, a welding plan that minimizes the number of welding pauses can be selected, reducing the chances of process errors and welding defects. Since the interpass temperature is recorded ahead of the welding torch in areas of relatively low and stable temperatures, it is not necessary to accurately represent the high-temperature gradients close to the torch itself in the thermal simulation.

## 2.3 Validation

### 2.3.1 Abaqus simulation

The thermal simulation was performed and compared with an Abaqus 2021 simulation (with implicit time integration) using the built-in features for AM. In the Abaqus simulation, a hemispherical Goldak [19] heat source of radius 1 mm was

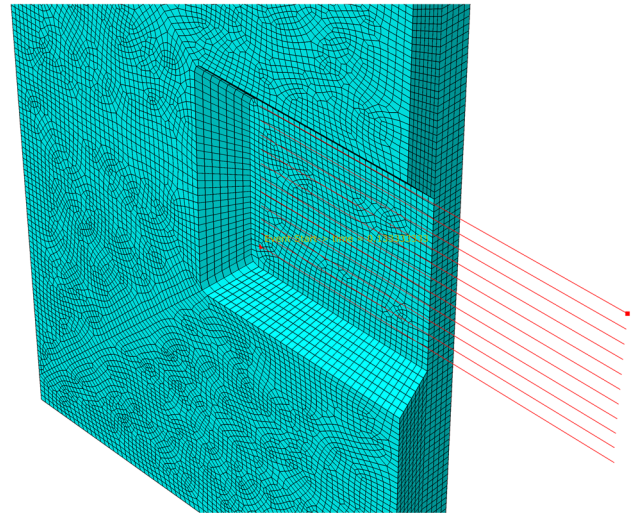


**Fig. 4** Half of Abaqus simulation model with infill welding paths displayed

used. Use of the Goldak heat source has been demonstrated successfully for similar applications [20]. The FE mesh consisted of hexahedral linear thermal elements (type DC3D8) with average edge lengths of 2 mm, yielding a model with around 248,000 elements. Figure 4 shows the (sectioned) Abaqus model and the welding paths. The analysis increment duration was locked at  $\Delta t = 0.1$  s.

In order to evaluate exclusively the performance of the element formulation in the WAAM repair planner, material deposition was turned off in the Abaqus simulation. Only the infill welding beads for the bottom layer of the repair of the test plate repair were simulated. In order to ensure equal timing of the welding in the two simulation methods, weld path decision-making was turned off in the WAAM repair simulator, and welding was instead simulated using fixed pauses between beads of 2 min.

Based on data from [21, 22], heat transfer and material properties representative of carbon steel were approximated to

$$h(T) = (10 + 0.12T) \text{ W}/(\text{m}^2\text{°C}), \quad (7)$$

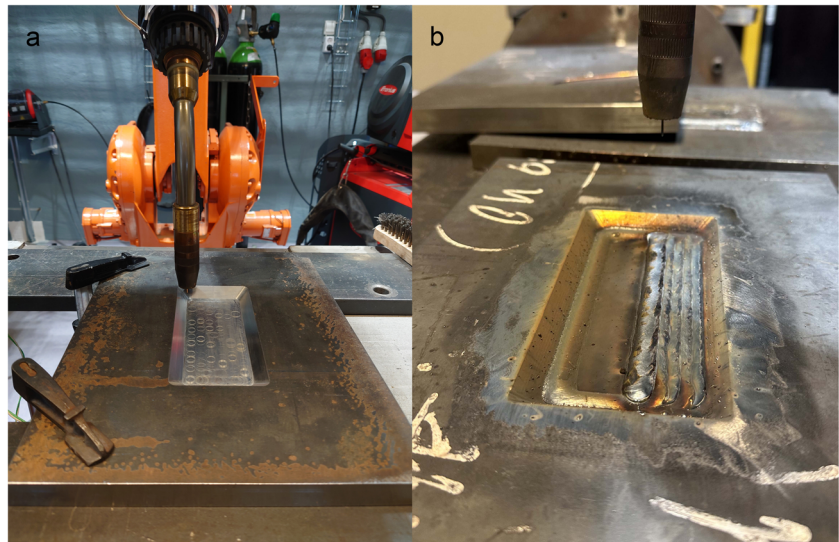
$$k(T) = \begin{cases} (54.7 - 0.0342T) \text{ W}/(\text{m}^{\circ}\text{C}), & \text{if } T < 800^{\circ}\text{C}, \\ 27.3 \text{ W}/(\text{m}^{\circ}\text{C}), & \text{if } T \geq 800^{\circ}\text{C}, \end{cases} \quad (8)$$

$$\rho = 7800 \text{ kg}/\text{m}^3, \quad (9)$$

$$c = 0.64 \text{ J}/(\text{g}^{\circ}\text{C}). \quad (10)$$

By changing these material parameters, the WAAM repair planner can be employed on other alloys in the future. In the current simulation, ambient and initial plate temperatures of 20 °C were assumed. The simulations used a welding speed of 6 mm/s and a heat input of 0.65 kJ/mm, as well as an

**Fig. 5** **a** Experimental setup showing a test plate, the robot and the welding torch. **b** Photograph taken during a pause in the physical welding test. One perimeter bead has been welded, and the robot is halfway through the first infill layer



arc energy of  $\eta = 0.8$  (according to recommendations in standard EN 1011-1:2009).

### 2.3.2 Experiment

A laboratory experiment was also conducted for validation of the thermal simulation. After machining a plate according to Fig. 1, the geometry was scanned, and welding paths were planned using three slices at  $-8.1$ ,  $-5.4$ , and  $-2.7$  mm below the top surface. The thermal simulation used parameters according to Eqs. 7, 8, 9 and 10, and pauses in the welding were added based on a maximum allowable interpass temperature of  $250$  °C.

The material of the test plate was VL E36 steel [23], a ship hull steel with similar composition and strength to S355, a conventional structural steel. Metal inert gas (MIG) pulse

welding was performed using  $\text{Ø}1.2$ -mm ESAB OK Autrod 13.23 welding wire and Corgon 18 shielding gas. The welding apparatus was Fronius TPS 400i mounted on an ABB IRB 2400 robot. The test plate was oriented horizontally with the welding torch in a vertical orientation (welding position PA). The welding speed was  $6$  mm/s, and heat inputs were between  $0.65$  and  $1.05$  kJ/mm. The long edges of the test plate were clamped to long steel beams during welding. The rest of the plate surface was exposed to air. Figure 5 shows the setup during welding.

A thermocouple was spot welded onto the backside of the test plate, at  $50$ - and  $20$ -mm distances in  $x$  and  $y$  directions from the center point that is shown in Fig. 1).

## 3 Results and discussion

### 3.1 Validation against Abaqus

Figure 6 shows the welding paths on a contour plot of the plate temperature produced by the WAAM repair simulator. From the temperature field, the temperature history of a virtual thermocouple in the center of the plate has been derived in Fig. 7. For validation, the temperature history of a virtual thermocouple on the backside of the Abaqus model is also shown. When the global, transient response is of primary interest, Fig. 7 shows that the WAAM repair simulator does an excellent job at providing just that. However, when the welding torch passes some point on the plate, steep through-thickness temperature gradients are present locally. Since the 2D WAAM repair simulator considers temperatures as constant across the plate thickness, the peak temperatures in the temperature history when the welding torch is near cannot be accurately represented. The temperature of the weld pool

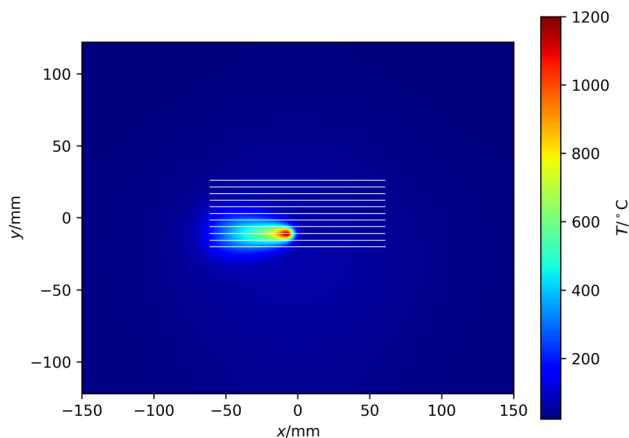


**Fig. 6** Contour plot of the calculated temperature field during the WAAM repair simulation that was performed for comparison with Abaqus. The simulated infill welding beads for the bottom layer of the repair of the test plate are shown as white lines

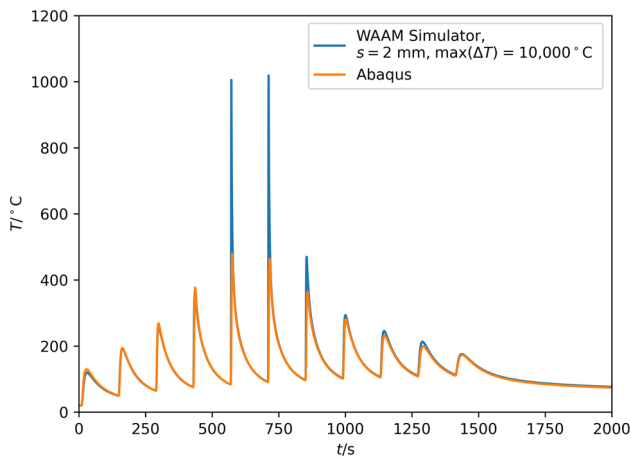


**Fig. 7** Temperature history for the center point at the back of the test plate calculated by the WAAM repair simulator and compared with that by Abaqus. In the WAAM repair simulation, the element size was  $s = 2$  mm, and the maximum allowable temperature change during a time increment was  $\max(\Delta T) = 10,000$  °C. In the Abaqus simulation, a time increment of  $\Delta t = 0.1$  s was used

in the contour plot in Fig. 6 is also unrealistically low since it represents an average temperature through the plate thickness.

For convergence checking, the Abaqus simulation was run again with an increased time increment from 0.1 to 1 s. The highest deviation in the temperature valleys, or minimum temperatures, in the temperature history, was 1.7 °C, which indicates that the solution presented in Fig. 7 is largely converged. The 0.1-s solution was used in further comparisons with the WAAM repair simulator.

In the WAAM repair simulator, equilateral elements with length  $s$  and a maximum allowable temperature change during a time increment,  $\max(\Delta T)$ , were used. To get a sufficient sampling rate of the welding torch position and power from the path plan, time increments were limited by the constraint  $\max(\Delta t) \leq 0.06$  s. Figure 8 shows the deviations in the minimum temperatures through the temperature histories in Fig. 7 for different values of  $s$  and  $\max(\Delta T)$ .  $\max(\Delta T) = 10$  °C can be considered a quite strict control on temperature change, whereas  $\max(\Delta T) = 10,000$  °C represents virtually no control for the relevant temperature ranges. From Fig. 7, some important observations can be made. Firstly, all the setups yielded very small deviations in the minimum temperatures compared to the Abaqus solution. Secondly, there was little variation between the different solutions, except for the  $s = 4$  mm,  $\max(\Delta T) = 10,000$  °C solution. For the other element sizes, the minimum temperatures were virtually identical for the  $\max(\Delta T) = 10$  °C and  $\max(\Delta T) = 10,000$  °C, since the latter setup was constrained by the maximum allowable time increment and produced constant time increments of  $\Delta t = 0.06$  s. Since

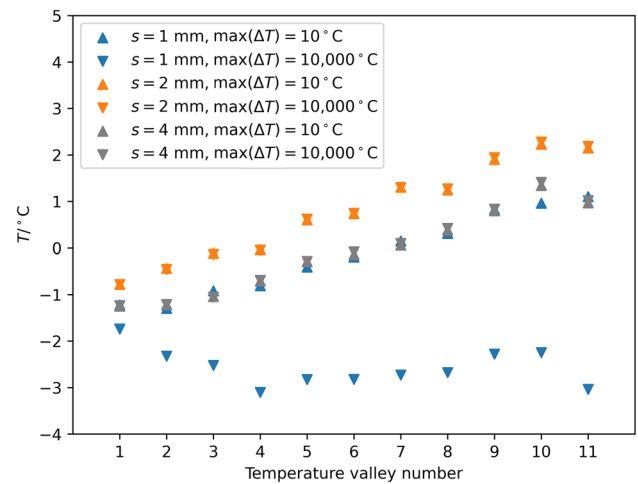


**Fig. 8** Plot of calculated temperatures by the WAAM repair simulator minus those calculated by Abaqus, for every temperature valley in Fig. 7

the  $s = 2$  mm,  $\max(\Delta T) = 10,000$  °C solution seemed converged, and this was used for further investigations.

Figure 9 shows the deviation in predicted temperature after the fifth peak in Fig. 7 between the WAAM repair simulator and Abaqus. The deviation is initially high but falls below 10 °C after only 7 s. This achievement is owed to the low through-thickness temperature gradients that are established quickly in regions of the plate that the welding torch has left behind in its path.

The computation time for the thermal simulation in the WAAM repair simulator was only 28 s when running on a single core on a 1.90-GHz Intel Core i7-8650U CPU. The simulation covered 2000 s in real time, where 224 s was with the welding torch turned on. In comparison, the Abaqus

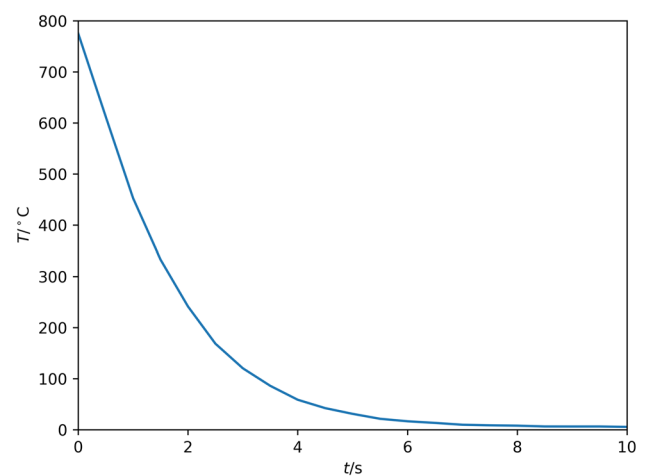


**Fig. 9** Temperature history after the fifth peak in Fig. 7 calculated by the WAAM repair simulator minus that calculated by Abaqus. For the WAAM simulator,  $s = 2$  mm and  $\max(\Delta T) = 10,000$  °C. The welding speed was 6 mm/s



simulation took 43 h on six processor cores for the  $\Delta t = 0.1$  s solution and 13 h on a single core for the  $\Delta t = 1$  s solution on a 3.00-GHz Intel Xeon Gold 6136 CPU. Thus, the WAAM repair simulator offers an immense saving in computational time. However, time usage in the Abaqus simulation could have been substantially decreased by employing similar types of dimensional and element-order reduction for the problem as had been employed in the WAAM repair simulator. Time usage for the WAAM repair simulator can be further decreased by increasing the maximum time increment. However, this would come at the cost of an increased error in welding torch position and power.

### 3.2 Validation against experiment

Figure 10 shows the temperature history measured by the thermocouple and calculated by the WAAM repair simulator. To take into account unexpected delays from the welding plan caused by ignition failures of the welding arc, as well as automatic adjustments in welding power made by the welding machine to produce stable arc conditions, the *logged* welding torch position and power were used as input for a rerun of the WAAM repair simulator. An accumulating, small, horizontal shift in extreme values between calculated and measured temperatures in Fig. 10 seems to indicate that perfect processing of the torch log file was not achieved. However, the temperature logs are well enough synchronized to make a comparison of minimum temperatures. Like in the comparison with the Abaqus simulation, the peak temperature predictions from the 2D WAAM repair simulator are higher than the temperatures measured on the back of the test plate when the torch is passing.

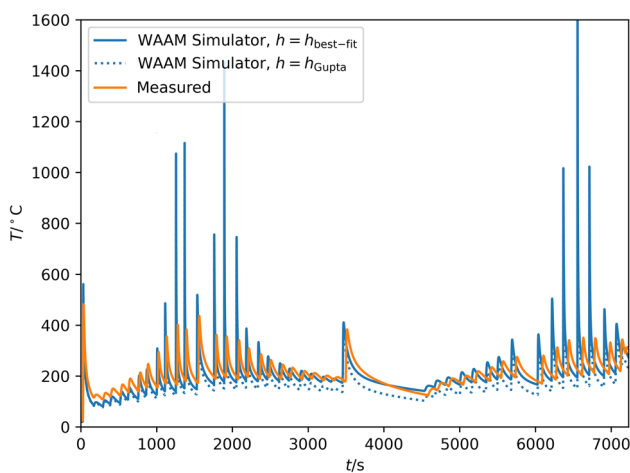


**Fig. 10** Temperature history calculated by the WAAM repair simulator ( $s = 2$  mm and  $\max(\Delta T) = 10,000$  °C) compared to that measured in a thermocouple on the backside of the test plate, 50 and 20 mm in  $x$  and  $y$  direction, respectively. The continuous temperature history for all welding layers is shown

The dotted, blue line in Fig. 10 shows the calculated temperature based on the heat transfer coefficient (HTC) from Eq. 7 measured by Gupta [22]. The HTC is a constant that scales the heat flux between a surface and a convective medium based on the temperature difference between them. Employing an HTC in a simulation represents a practical yet very simplified way of taking into account the complex phenomena of convection and airflow. Since convective conditions on a component can vary considerably depending on its orientation and geometrical features [24], a best-fit HTC was also calibrated this particular thermal history, by minimizing the difference between simulated and measured minimum temperatures between the weld beads. The resulting linear relation,

$$h(T) = 0.11T \text{ W}/(\text{m}^2\text{°C}), \tag{11}$$

is slightly lower than Eq. 7 and is believed to be applicable for welding on similar geometrical setups.

From Fig. 10, the best-fit simulation seems to capture the trend in measured minimum temperatures very well. The good correspondence for this relatively complex temperature history demonstrates the validity of the approach, and the authors believe it will be applicable to other welding cases on thin-walled components. If the calculation of material deposition during welding is implemented in the WAAM repair simulator, accuracy can likely be further increased.

Finally, the log from the welding path decision maker is also shown in Fig. 11. The blue line shows the temperature measured ahead of the welding torch. The welding torch will always be turned off before the torch can enter an area where the temperature is above the interpass temperature

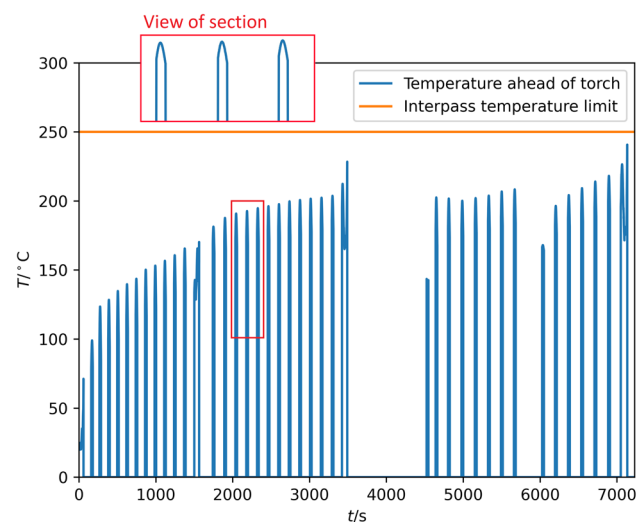


**Fig. 11** Temperature in front of the welding source calculated with the WAAM simulator compared to the interpass temperature limit

limit. Logging in front of the torch is also turned off when the torch is turned off, resulting in no plotted temperature during breaks in Fig. 11. During breaks, the heat in the plate will assume a centered distribution, since heat transfer on the edges of the plate is limited, and since heat is diffusing out in the plate from relatively centralized preceding weld beads. Thus, the curves for measured temperatures ahead of the torch will peak roughly midway through each pass, when the  $x = 0$  line in the plate is passed, as shown in the section view in Fig. 11.

During the laboratory test, there were two welding arc ignition failures, which can be observed in Fig. 11 as extended breaks starting at around  $t = 3500$  and  $t = 5700$  s, respectively. Except for the weld beads that were directly influenced by these unexpected delays, the repair operation was carried while keeping the interpass temperature below, yet quite close to, the allowed limit. This shows that employing a high and low temperature limit to the simulation can be an effective way to maximize the utilization of the allowed operational window, in order to minimize operational time. Even compared to processing thermocouple measurements live during a repair, use of the WAAM repair simulator can offer advantages, e.g., the capability of performing a moving interpass temperature evaluation, or absolute minimization of operational time by employment of a sophisticated thermal management/timing strategy for the repair *as a whole*. The physics-based model for such optimization is provided by the current work.

## 4 Future work

Some suggestions for possible further development of the WAAM repair simulator are outlined below.

- Update the thickness,  $d(i, j)$ , when welding. This can be used to predict the building height based on the welding path plans. It can also enable a more accurate calibration of the thermal simulation since the heat capacity of the added material is taken into account in Eq. 6.
- Adapt the welding path planner and thermal simulation to cylinder coordinates for application to pipelines. In the thermal simulation, element volume and surface areas would have to be calculated based on the pipe wall curvature and thickness. For small-diameter pipes, a “virtual seam”—that is, connectivity between elements at the 0 and 360° position—can be implemented to model heat transfer around the circumference of the pipe accurately.
- Employ and validate thermal simulation to condition with different media on each side of the wall, like the flowing medium in a subsea pipeline in service.
- Treat the shielding gas in the habitat as a heat sink *of finite capacity* and use Eq. 4 to estimate the heat exchange

and gas temperature. Such calculations can be used to prevent damage to equipment in contact with the gas due to overheating.

- Loop through the thermal simulation and decision making in Algorithm 1 with different values of the low temperature limit in line 34. The results can be used to select the low limit that yields the lowest process time.
- For large damaged geometries, the torch can be moved to another location with a lower temperature instead of pausing the welding. Implementing an algorithm for this may result in reduced process time.
- For increased accuracy in the thermal simulation, include temperature dependency in the heat capacity,  $c = c(T)$ .

## 5 Conclusions

A welding path planner, a 2D thermal simulation, and a decision-making tool for WAAM repair of thin-walled structure have been presented. The 2D simulation approach has been validated as a viable calculation method if the global temperature field is of interest. Since the thickness dimension is not modeled, only the average temperature across the wall thickness is calculated. Thus, the approach is not accurate for representing peak temperatures near the welding torch. However, as the welding torch moves away, the temperature field quickly assumes a 2D state. For a model with equilateral elements of length 2 mm, the temperature deviation in a location compared to Abaqus was less than 10 °C only 7 s after the welding torch had passed. Thus, the approach provides an accurate overview of the global temperatures in a structure and is used in the current work to produce a welding plan that complies with a maximum allowable interpass temperature limit.

The approach allows for fast planning and evaluation of repair of thin-walled structures, for both subsea and onshore applications. The current work simulated a 2000-s welding operation in only 28 s. As the approach uses a wall thickness field derived directly from an aligned 3D scan, the approach has the added advantage of saving time on manual modeling work. Several future activities to increase the accuracy and extend the functionality of the approach have been proposed.

**Acknowledgements** The authors want to thank Geir Ole Tysse, Morten Høgseth Danielsen, Philippe E. Mainçon, Marius E. H. Andersen, Ragnhild Aune (all SINTEF), Steinar Gregersen (Kongsberg Ferrotech), and Lars M. Haldorsen (Equinor Energy) for helpful discussions on the WAAM repair simulator.

**Author Contributions** Conceptualization: PQ, EBN, TB, XR. Methodology: PQ, EBN. Software: PQ, EBN. Validation: PQ, EBN. Formal analysis and investigation: PQ, EBN. Writing—original draft preparation: PQ, EBN, TB, XR. Writing—review and editing: PQ, EBN, TB, XR. Visualization: PQ, EBN. Project administration: TB. Funding acquisition: EBN, TB, XR

**Funding** Open access funding provided by SINTEF. The authors received funding from Kongsberg Ferrotech AS, Equinor Energy AS and Gassco AS through the project IPN SAMLE, Research Council of Norway grant number 317838.

## Declarations

**Conflict of interest** The authors declare no competing interests.

**Open Access** This article is licensed under a Creative Commons Attribution 4.0 International License, which permits use, sharing, adaptation, distribution and reproduction in any medium or format, as long as you give appropriate credit to the original author(s) and the source, provide a link to the Creative Commons licence, and indicate if changes were made. The images or other third party material in this article are included in the article's Creative Commons licence, unless indicated otherwise in a credit line to the material. If material is not included in the article's Creative Commons licence and your intended use is not permitted by statutory regulation or exceeds the permitted use, you will need to obtain permission directly from the copyright holder. To view a copy of this licence, visit <http://creativecommons.org/licenses/by/4.0/>.

## References

- Fostervoll H, Woodward N, Akselsen OM (2009) The effects on process performance of reducing the pressure from 36 to 1 bar in hyperbaric MIG welding. International Conference on Off-shore Mechanics and Arctic Engineering, vol 3: Pipeline and Riser Technology, pp 197–205. <https://doi.org/10.1115/OMAE2009-79291>
- Williams SW, Martina F, Addison AC, Ding J, Pardal G, Colegrove P (2016) Wire + arc additive manufacturing. Mater Sci Tech 32(7):641–647. <https://doi.org/10.1179/1743284715Y.0000000073>
- Wu B, Pan Z, Ding D, Cuiuri D, Li H, Xu J, Norrish J (2018) A review of the wire arc additive manufacturing of metals: properties, defects and quality improvement. J Manuf Process 35:127–139. <https://doi.org/10.1016/j.jmapro.2018.08.001>
- Priarone PC, Campatelli G, Catalano AR, Baffa F (2021) Life-cycle energy and carbon saving potential of wire arc additive manufacturing for the repair of mold inserts. CIRP J Manuf Sci Tec 35:943–958. <https://doi.org/10.1016/j.cirpj.2021.10.007>
- Dassault Systèmes (2023) Simulia user assistance 2023 – Abaqus. Dassault Systèmes
- Hexagon AB (2022) Simufact additive 2022 – introducing simufact additive. Hexagon AB
- Buhl J, Israr R, Bambach M (2019) Modeling and convergence analysis of directed energy deposition simulations with hybrid implicit/explicit and implicit solutions. J Mach Eng 19:94–107. <https://doi.org/10.5604/01.3001.0013.4086>
- Ding J, Colegrove P, Mehnen J, Williams S, Wang F, Almeida PS (2014) A computationally efficient finite element model of wire and arc additive manufacture. Int J Adv Manuf Tech 70:227–236. <https://doi.org/10.1007/s00170-013-5261-x>
- Sun L, Ren X, He J, Olsen JS, Pallaspuro S, Zhang Z (2019) A new method to estimate the residual stresses in additive manufacturing characterized by point heat source. Int J Adv Manuf Tech 105:2415–2429. <https://doi.org/10.1007/s00170-019-04443-1>
- Sun L, Ren X, He J, Zhang Z (2021) A bead sequence-driven deposition pattern evaluation criterion for lowering residual stresses in additive manufacturing. Addit Manuf 48:102424. <https://doi.org/10.1016/j.addma.2021.102424>
- Weisz-Patrault D (2020) Fast simulation of temperature and phase transitions in directed energy deposition additive manufacturing. Addit Manuf 31:100990. <https://doi.org/10.1016/j.addma.2019.100990>
- Le VT, Nguyen HD, Bui MC, Pham TQD, Le HT, Tran VX, Tran HS (2022) Rapid and accurate prediction of temperature evolution in wire plus arc additive manufacturing using feedforward neural network. Manuf Lett 32:28–31. <https://doi.org/10.1016/j.mfglet.2022.02.003>
- Sun J, Klassen J, Nitschke-Pagel T, Dilger K (2018) Effects of heat source geometric parameters and arc efficiency on welding temperature field, residual stress, and distortion in thin-plate full-penetration welds. Int J Adv Manuf Tech 99:497–515. <https://doi.org/10.1007/s00170-018-2516-6>
- Montevecchi F, Venturini G, Grossi N, Scippa A, Campatelli G (2018) Idle time selection for wire-arc additive manufacturing: a finite element-based technique. Addit Manuf 21:479–486. <https://doi.org/10.1016/j.addma.2018.01.007>
- American Welding Society (2010) D1.1/D1.1M:2010 (2nd printing) Structural welding code-steel. American Welding Society
- American Petroleum Institute (2016) API RP 582: recommended practice welding guidelines for the chemical, oil, and gas industries, 3rd ed. American Petroleum Institute
- Dornelas PHG, Farias FWC, e Oliveira VHPM, de Oliveira Moraes D, Júnior PZ, da Cruz Payão Filho J (2020) Influence of welding interpass temperature on Charpy V-notch impact energy of coarse-grain heat-affected zone of AISI 4130 steel pipe. Int J Adv Manuf Tech 108(7):2197–2211. <https://doi.org/10.1007/s00170-020-05542-0>
- Wang XL, Tsai TYT, Yang JR, Wang ZQ, Li XC, Shang CJ, Misra RDK (2017) Effect of interpass temperature on the microstructure and mechanical properties of multi-pass weld metal in a 550-MPa-grade offshore engineering steel. Weld World 61(6):1155–1168. <https://doi.org/10.1007/s40194-017-0498-x>
- Goldak J, Chakravarti A, Bibby M (1984) A new finite element model for welding heat sources. Metall Trans B 15(2):299–305. <https://doi.org/10.1007/BF02667333>
- Farias RM, Teixeira PRF, Vilarinho LO (2021) An efficient computational approach for heat source optimization in numerical simulations of arc welding processes. J Constr Steel Res 176:106382. <https://doi.org/10.1016/j.jcsr.2020.106382>
- Franssen J-M, Vila Real P (2016) Annex a: thermal data for carbon steel and stainless steel sections. John Wiley & Sons, Ltd, ???, pp 369–394. <https://doi.org/10.1002/9783433607008.app1>
- Gupta SM (1977) Measurement of quench heat transfer coefficients and their use in heat treatment design. Master's thesis, University of British Columbia
- DNV GL AS (2015) Offshore Standard DNVGL-OS-B101 – Metallic materials. DNV GL AS
- Huang R-T, Sheu W-J, Wang C-C (2008) Orientation effect on natural convective performance of square pin fin heat sinks. Int J Heat Mass Tran 51(9):2368–2376. <https://doi.org/10.1016/j.ijheatmasstransfer.2007.08.014>

**Publisher's Note** Springer Nature remains neutral with regard to jurisdictional claims in published maps and institutional affiliations.